Active site recovery and N-N bond breakage during hydrazine oxidation boosting the electrochemical hydrogen production

Libo Zhu
Shanghai Institute of Ceramics Chinese Academy of Sciences
Jian Huang
Search Results Web Result with Site Links Shanghai Institute of Ceramics, Chinese Academy of Sciences
Ge Meng
Shanghai Institute of Ceramics
Tiantian Wu
Shanghai Institute of Ceramics Chinese Academy of Sciences
Chang Chen
Shanghai Institute of Ceramics
Han Tian
State Key Laboratory of High Performance Ceramics and Superfine Microstructures, Shanghai Institute of Ceramics, Chinese Academy of Sciences
Yafeng Chen
Shanghai Institute of Ceramics
Fantao Kong
Shanghai Institute of Ceramics, Chinese Academy of Sciences
Ziwei Chang
School of Physical Science and Technology, Shanghai Tech University
Xiangzhi Cui
Shanghai Institute of Ceramics
Jianlin Shi (jlshi@mail.sic.ac.cn)
Shanghai Institute of Ceramics Chinese Academy of Sciences https://orcid.org/0000-0001-8790-195X

Article

Keywords: hydrogen evolution reaction, hydrazine oxidation reaction, bimetallic phosphide, electrocatalysis mechanism, electrochemical utilization ratio

Posted Date: August 25th, 2022

DOI: https://doi.org/10.21203/rs.3.rs-1965916/v1

Version of Record: A version of this preprint was published at Nature Communications on April 10th, 2023. See the published version at https://doi.org/10.1038/s41467-023-37618-2.

Abstract

Using hydrazine oxidation reaction (HzOR) substituting for oxygen evolution reaction can realize hydrogen production at largely reduced energy consumption. While the HzOR mechanism and the electrochemical utilization rate of hydrazine are still ambiguous. Herein, a bimetallic phosphide heterostructure nanoarrays (Ni-Co-P/NF) fabricated by an interface engineering strategy was used to catalyze both HzOR and hydrogen evolution reaction (HER), and more intensively, probe the HzOR mechanism. The extra-high HzOR performance is attributed to the instantaneous recovery of metal phosphide active site by hydrazine and the extremely low energy barrier with even a new HzOR pathway of N-N bond breakage, which enables the electrolyzer catalyzed by Ni-Co-P/NF to reach 500 mA cm^{-2} for H_2 production at as low as 0.498 V, and offers a high hydrazine electrochemical utilization rate of 93%. The constructed electrolyzer can be powered by the direct hydrazine fuel cell with Ni-Co-P/NF as anodic catalyst, achieving self-powered hydrogen production at the rate up to 19.6 mol h^{-1} m^{-2}.

Introduction

Electro overall water splitting (OWS) is an efficient approach to obtain high purity hydrogen by using clean energy such as wind and solar energy[1]. However, the anodic oxygen evolution reaction (OER) in OWS is kinetically slow, which necessitates high electrolytic potential and large amount of expensive catalyst to overcome the gigantic reaction energy barrier[2,3]. Thus, alternative strategies have been developed to reduce the energy input for OWS. Coupling the electrocatalytic oxidation of the small molecules with low reaction energy barrier, such as methanol[4], ethanol[5], formic acid[6], hydrazine (N_2H_4) and urea, etc.[7] in the anodic chamber is one of the effective strategies to reduce the energy consumption for hydrogen evolution reaction (HER)[8,9], which could concurrently electro-synthesize the high valued products.

Among various small molecule oxidation reactions, hydrazine oxidation reaction (HzOR, $N_2H_4 + 4OH^- \rightarrow N_2 + 4H_2O + 4e^-$, -0.33 V vs. RHE) with absolute carbon free products and less catalyst poisoning, is an ideal energy-saving substitute for OER (1.23 V vs. RHE) [10,11]. Unfortunately, however, N_2H_4 trends to decompose directly to form N_2 and H_2 ($N_2H_4 \rightarrow N_2 + 2H_2$), which would reduce the electrochemical utilization rate of N_2H_4[12,13]. Thus, designing efficient and low-cost HzOR electrocatalysts to enhance the electrochemical utilization rate of N_2H_4 is of great significance to achieve low energy consumption and high efficiency for hydrogen production.

Recently, the HzOR electrocatalysts have been investigated extensively including the Pt based noble metal[14,15] and transition metal based catalysts[16–21]. Among these electrocatalysts, nickel phosphide has been reported to be the efficient catalyst toward HzOR because of its advantages of high chemical stability and excellent conductivity[17–22]. However, the HzOR/HER performances under high current density are not satisfactory due to the limited gas-solid-liquid three-phase reaction interface at the

catalyst. Most recently, three-dimensional (3D) nanoarrays structure has been reported to be feasible for enhancing the HzOR/HER catalytic performances because of its high exposed active sites, excellent hydrophilicity as well as the fast charge/mass transfer ability[23,24]. Though the HzOR/HER performances are elevated at a certain degree[25,26], the catalytic mechanism probing of the most reports still focuses on HER, while the HzOR of 4-electron transfer process, which is important to enhance the electrochemical utilization rate of N_2H_4 in the anode chamber, has been little known, leading to the ambiguous HzOR active centers and indeterminate reaction path of HzOR[27].

Herein, a 3D nickel cobalt phosphide heterostructure nanoarrays on nickel foam (Ni-Co-P/NF) with CoP nanoparticles uniformly distributed outside of the NiCoP nanowires was fabricated by an interface engineering strategy and used as a probe catalyst to reveal the HzOR mechanism and elevate the electrochemical utilization rate of N_2H_4 as well. The heterostructure nanoarrays and the hydrophilic/hydrophobic interface structure endow the Ni-Co-P/NF bifunctional catalyst with much enhanced activities toward both HER and HzOR, especially, only 176 mV is needed to reach an extra-high current density of 1000 $mAcm^{-2}$ for HzOR. The excellent electrochemical activity of Ni-Co-P/NF heterostructure nanoarrays originates from the interface electron transfer between CoP nanoparticles and the NiCoP nanowires, resulting in the extremely low energy barrier of HzOR and even a new reaction path of N-N bond breakage at 0.2 V or above. Additionally, the *in situ* formed MPO_x (metal phosphorus oxide) resulting from the electrochemical oxidation of Ni-Co-P/NF in anodic chamber can be instantly recovered to active MP (metal phosphide) species during HzOR. Resultantly, the voltage input of the electrolyzer equipped with Ni-Co-P/NF catalysts for both HER and HzOR is as low as 0.88 V to reach 200 $mAcm^{-2}$, 1.04 V lower than that of OWS (1.92 V), greatly reducing the energy consumption. Especially, the N_2H_4 electrochemical utilization rate reaches 93% by optimizing the N_2H_4 concentration. Furthermore, the electrolyzer can be powered by the self-assembled direct hydrazine fuel cell (DHzFC) using Ni-Co-P/NF as anodic catalyst for HzOR, realizing self-powered hydrogen production at a rate up to 19.6 mol h^{-1} m^{-2} without external electricity supply.

Results And Discussion

Catalyst characterization. The Ni-Co-P heterostructure nanoarrays with CoP nanoparticles uniformly distributed on the surface of NiCoP nanowires were *in situ* synthesized on nickel foam (NF) by ion exchange method as shown in Fig. S1, in which the NF is corroded and oxidized to Ni (II) during the hydrothermal synthesis to form Ni-Co precursor nanoarrays on NF (Ni-Co-Pre/NF), and then the Ni-Co-P/NF was synthesized after phosphating by using NaH_2PO_2[28,29].

The Ni-Co-Pre/NF shows a nanowire array morphology of 900 nm in an average length on NF (Fig. 1a, Fig. S2). With the increase of Co source addition amount from 3 to 5 mmol, the nanowire arrays of Ni-Co-Pre/NF gradually accumulate into a sea urchin shape (Fig. S3a and S3b), which adhere on the NF substrate loosely and will easily fall off in subsequent treatment. 3 mmol cobalt source addition amount is optimal, at which the precursor loading on NF achieves maximum according to the XRD patterns and

the digital photographs (Fig. S3c). After phosphating, sample Ni-Co-P/NF at the optimal Co source addition of 3 mmol retains the dense and uniform 3D nanowire morphology of precursor (Fig. 1b, Fig. S4), while the surface becomes rougher because of a large number of nanoparticles formed on the surface of nanowires (inset in Fig. 1b). Moreover, the nanoarrays of Ni-Co-P/NF are hydrophilic featuring a much lower water contact angle (36.14°) than that of Pt/C (139.98°) (Fig. S5), which is favorable for the release of absorbed bubbles on discontinuous solid-liquid-gas triple phase contact points[30].

In the TEM and high-resolution TEM (HRTEM) images (Fig. 1c and 1d), two different morphologies in Ni-Co-P (the sample separated from NF) were observed: randomly oriented particles from nanowire under ultrasound (area 1) (Fig. 1d) with the selected area electron diffraction (SAED) pattern being assignable to CoP with (011) (211) (013) planes (Fig. 1d illustration), and nanowire main phases (area 2) (Fig. 1e). The energy dispersion spectrum (EDS) (Fig. S6) indicates the component ratio of area 1 is Co:P = 1:1 and that of area 2 is Ni:Co:P = 1:1:1, further confirming the existence of CoP in area 1 and nickel cobalt phosphide (NiCoP) in area 2. While the edge area of the nanowire (Fig. 1e) is Co-rich and Ni-deficient besides P signal according to the element linear scanning profile in Fig. S7, evidencing the existence of CoP nanoparticles outside of the NiCoP nanowires. In addition, the oxygen signal can also be detected, indicating the partial oxidation of the outer layer into an amorphous phosphorus oxide layer[31]. Two sets of interplanar spacing of 0.202 nm and 0.285 nm can be detected in HRTEM (Fig. 1f), which are in correspondence to the (201) plane of NiCoP and (011) plane of CoP, respectively, indicating the successful synthesis of Ni-Co-P heterostructure nanoarrays with CoP nanoparticles uniformly distributed outside of the NiCoP nanowires in Ni-Co-P/NF (Fig. S8). The element mappings in Fig. 1g demonstrate the homogeneous dispersion of Co, Ni, P on nanowires, while Co is slightly wider than that of Ni, further indicating successful loading of CoP nanoparticles on the NiCoP nanowires surface.

From the XRD patterns in Fig. 2a, the strongest diffraction peaks of Ni-Co-P/NF centered at 40.99°, 44.90° (covered by nickel peaks), and 47.58° can be indexed to the (111), (201), (210) planes of standard hexagonal NiCoP (JCPDS No. 71-2336), and those at 31.59°, 36.32°, 48.12° assigned to the (011), (111), (211) planes of CoP (JCPDS No. 29–0497), further verifying the formation of Ni-Co-P heterostructure nanoarrays on NF with CoP nanoparticles distributed outside of the NiCoP nanowires[32].

The survey scan of XPS spectrum of the Ni-Co-P/NF indicates the existence of Co, Ni, P, and O element (Fig. S9). Co 2p XPS spectra (Fig. 2b) of Ni-Co-P/NF exhibits two major groups with binding energies of 778.7 and 793.5 eV, respectively, representing Co-P, which are close to those of metallic Co (778.2 and 793.3 eV), indicating the presence of partially charged Co species ($Co^{\delta+}$, δ is close to 0). While the relatively weak bands at 781.8 and 797.6 eV belong to the Co-PO_x resulting from the Co oxidation state, and the 785.6 and 802.5 eV are the satellite peak of Co. Similarly, there are three groups of peaks appear in the Ni 2p XPS spectra (Fig. 2c), and the binding energies at 853.6 and 870.8 eV represent Ni-P ($Ni^{\delta+}$), and those at 56.8 and 874.7 eV belong to Ni-PO*x*, and the 861.3 and 879.6 eV are assigned to the satellite peak of Ni[33–36]. Compared to CoP, the Co 2p3/2 and 2p1/2 of Ni-Co-P/NF slightly shift toward the lower binding energies (Fig. 2b, 2c, Fig. S9), while the Ni 2p3/2 and 2p1/2 of Ni-Co-P/NF have a higher binding

energy shift compared NiP/NF, indicating an increased ionicity of M − P bond in bimetallic phosphides and a promoted electron migration from metal to phosphide[37], which makes the electronic structure of the Ni-Co-P more conducive to the HER and HzOR. The deconvoluted P XPS peaks (Fig. 2d) at 128.3 and 130.2 eV belong to P 2p1/2 and P 2p3/2 of MP, which is lower than that of elemental P (130.0 eV), suggesting that the P is partially negatively charged ($P^{\delta-}$), and the peak at 133.5 eV could be ascribed to a metallic oxidation state, which is associated with MPO_x due to exposed to the air[38]. In addition, the binding energies of P in MP and MPO_x in Ni-Co-P/NF also shift to the lower position compared with those of NiP/NF and CoP, indicating the electron-rich character of P. Thus, the P can trap positively charged protons during electrocatalysis, which is responsible for the HER activity[39].

X-ray absorption fine structure (XAFS) spectrum was obtained to investigate the local electronic structure and atomic arrangement of Co K-edge and Ni K-edge. In the normalized X-ray absorption near edge structure (XANES) (Fig. 2e), the absorption edge energy of Co K-edge in Ni-Co-P/NF is in between those of CoO and Co foil (Fig. 2g-left), and similar to that of CoP, indicating that the average value state of Co element is in between 0 and + 2, consistent with the XPS results[35]. Similarly, the absorption edge energy of Ni K-edge of Ni-Co-P/NF gives the average value states of Ni between 0 and + 2 (Fig. 2f), slightly higher than that of NiP according to Fig. 2g-right, suggesting the changed binding energy between Ni and P due to the electronic interaction between Co and Ni. The Fourier-transformed extended X-ray absorption fine structure (EXAFS) spectrum of Ni-Co-P/NF shows the similar radial distribution function to those of CoP and NiP as shown in Fig. 2h and Fig. 2i, respectively. Relative to the reference CoP, a similar peak at the 1.66 Å in Ni-Co-P/NF is assigned to Co − P bond because of the existence of CoP species in Ni-Co-P/NF (Fig. 2h). Notably, the Ni − P peak in Ni-Co-P/NF positively shifts to 1.75 compared to 1.69 Å in NiP reference (Fig. 2i), due to the Co introduction. All above results demonstrate the interaction between Ni and Co atoms in NiCoP lattice and the coexistence of CoP and NiCoP components.

Electrocatalytic HER performance. The HER electrocatalytic activity of the as-synthesized catalysts were investigated in N_2-saturated 1.0 M KOH electrolyte, which was calibrated by reversible hydrogen electrode (RHE) as shown in Fig. S10. From the linear sweep voltammetry (LSV) curves in Fig. 3a, sample Ni-Co-P/NF requires a much lower overpotential (37 mV) to reach 10 mA cm^{-2} compared to references NiP/NF (124 mV), Ni-Co-Pre/NF (175 mV), and CoP (173 mV). Though the overpotential of Ni-Co-P/NF below 150 mA cm^{-2} is slightly higher than that of the Pt-C/NF (η_{10} = 28 mV), but become substantially lower than that of Pt-C/NF at current density above 150 mA cm^{-2}. Importantly, the Ni-Co-P/NF catalyst needs only 280 mV to reach 1000 mA cm^{-2}, which is better than most reported catalysts (Table S1). A Tafel slope of 33.3 mV dec^{-1} was recorded on Ni-Co-P/NF (Fig. 3b), much smaller than those of NiP/NF (84.0 mV dec^{-1}), Ni-Co-Pre/NF (129.3 mV dec^{-1}), and CoP (72.6 mV dec^{-1}), though slightly larger than 23.6 mV dec^{-1} of Pt-C/NF in the potential range[40], suggesting the Tafel mechanism dominated the reaction on Ni-Co-P/NF.

The electrochemical resistance spectra (EIS) of the catalysts are shown in Fig. 3c, and the resistance of Ni-Co-P/NF (13.09 Ω) is much lower than those of CoP (57.3Ω) and NiP/NF (45.9Ω) though slightly

higher than that of the Pt-C/NF (10.73 Ω) according to the fitting data in Table S2. Since the electrochemical double-layer capacitance (C_{dl}) of the catalyst is proportional to its electrochemical active surface area (ECSA) directly related to catalytic activity, Ni-Co-P/NF shows the C_{dl} value of 20.6 mF cm^{-2} (Fig. 3d and Fig. S11), much higher than Ni-Co-Pre/NF (10.6 mF cm^{-2}), NF (2.2 mF cm^{-2}), and Pt-C/NF (2.2 mF cm^{-2}), indicating the highest ECSA of Ni-Co-P/NF heterostructure nanoarrays than others.

In addition, the Ni-Co-P/NF shows excellent HER catalytic stability, which can be operated stably for 90 h at -50 mV with a limited current attenuation by 6.7% at the end of test (Fig. 3e). The accelerated durability tests (ADTs) in Fig. S12 show no significant change in LSV curves after 10000 cycles, further confirming the excellent stability of Ni-Co-P/NF toward HER. Furthermore, the influence of Co addition on the HER performance of Ni-Co-P/NF composite was also tested (Fig. S13), and the Co-3 with $Co(NO_3)_2{\cdot}6H_2O$ addition of 3 mmol during the synthesis (as named Ni-Co-P/NF above) is optimal for HER catalytic activity. Moreover, the volume of H_2 production was collected by gas chromatography (GC) and compared with the theoretical gas volume obtained from the number of transferred electrons, which gives a HER Faradaic efficiency (FE) of 97.2% on Ni-Co-P/NF (Fig. S14).

Electrocatalytic HzOR performance. The HzOR electrocatalytic activity of the as-synthesized catalysts was tested in an aqueous electrolyte containing 1.0 M KOH and 0.1 M N_2H_4 using a typical three-electrode system. Figure 4a exhibits the LSV curves with 90% iR compensation at the scan rate of 50 mV s^{-1}. Compared to NiP/NF (20 mV), CoP (-3 mV) and Ni-Co-Pre/NF (260 mV), sample Ni-Co-P/NF requires a much lower potential (-61 mV) to reach a current density of 10 mA cm^{-2}, which is superior to the Pt-C/NF (34 mV). Exceptionally, the ultralow working potentials of -24, 78 and 176 mV are required for Ni-Co-P/NF heterostructure nanoarrays to reach current densities of 100, 500 and 1000 mA cm^{-2}, respectively. From Fig. 4b, Ni-Co-P/NF shows a small Tafel slope of 22.9 mV dec^{-1}, largely lower than those of Pt-C/NF (33.2 mV dec^{-1}), NiP/NF (49.5 mV dec^{-1}) and CoP (92.5 mV dec^{-1}), indicating its fast catalytic kinetics for HzOR. The excellent HzOR catalytic activity of Ni-Co-P/NF is connected with its much smaller electrochemical resistance. In the simulated equivalent circuit diagram in the inset of Fig. 4c, R_s, R_f and R_{ct} respectively represent the solution resistance, high-frequency semicircle resistance and the charge-transfer resistance, and the Q_{CPE1} and Q_{CPE2} were introduced to simulate the double-layered capacitor at catalyst interface and the electrode/electrolyte interface, respectively[41]. According to the result of EIS and model fitting (Table S3), Ni-Co-P/NF shows the lowest R_{ct} (2.614 Ω) and R_f (0.990 Ω) values owing to its three dimensional array structure having greatly increased contact area at gas-solid-liquid three-phase, in which the N_2H_4 molecules adsorbed on the catalyst surface and electrolyte can be oxidized immediately and continuously, meanwhile the electrons generated can be efficiently transferred through conductive NF.

Figure 4d gives the comparison between HzOR by Ni-Co-P/NF (in 1.0 M KOH and 0.1 M N_2H_4) and OER by RuO_2 catalyst (in 1.0 M KOH). An ultralow potential of 90 mV is required for Ni-Co-P/NF to reach an elevated current density of 200 mA cm^{-2}, which is 1.54 V lower than that of RuO_2 catalyst (1.63 V) at the

same current density, suggesting the significantly reduced energy consumption for hydrogen production by replacing OER with HzOR. To further investigate the HzOR kinetics for Ni-Co-P/NF, varied scanning rates were adopted. It can be seen from Fig. 4e that the current changes in LSV curves are negligible at the varied scanning rates from 10 to 50 mV s^{-1}, suggesting the efficient charge and mass transfer at the electrode-electrolyte-gas three-phase interface on Ni-Co-P/NF, and resultantly, the fast HzOR kinetics. The Ni-Co-P/NF with Co source addition of 3 mmol shows the best HzOR performance (Fig. S15), coincident with the best HER activity. Moreover, the LSV curve of Ni-Co-P/NF after 10000 cycles shows no significant shifts compared to the initial cycle according to the ADTs (Fig. 4f), indicating its excellent catalytic stability. From the i-t test of Ni-Co-P/NF toward HzOR (Fig. 4g), a large current density above 100 $mAcm^{-2}$ can be retained, which is 91% of the initial value at the end of 100 h. Furthermore, the phase structure, composition and morphology of the Ni-Co-P/NF catalyst after stability test (name as Ni-Co-P/NF-used) remain almost unchanged after the test according to the XRD patterns (Fig. S16), Raman spectra (Fig. S17)[42] and TEM images (Fig. S18), further confirming the excellent HzOR catalytic stability of Ni-Co-P/NF heterostructure nanoarrays. The HzOR activity parameters of Ni-Co-P/NF, such as the potential to reach 100 $mAcm^{-2}$ and Tafel slope in this study, are even better than those of the most reported non-noble metal-based catalysts (Fig. 4h, Table S4).

HzOR mechanistic insight. Based on above results, the HzOR catalytic mechanism of the obtained catalyst was investigated. The CV measurements on Ni-Co-P/NF electrode were firstly carried out in the voltage range of -0.2 V to 0.4 V in 1 M KOH and − 0.2 V to 0.8 V in 1.0 M KOH + 0.1 M N_2H_4 to determine the active sites of bimetallic phosphides and the potential changes on HzOR (Fig. 5a). A pair of redox peaks, A_1 and B_1 on the dotted blue CV curve, corresponds to the conversion between MPO_x (the valence state of M is in between + 2 and + 3) and MP (M: δ^+, δ is close to 0) in the 1 M KOH, indicating the surface oxidation/reduction of the metal phosphide in the anodic oxidation range as shown in Eq. (1).

$$MP + OH^- \leftrightarrow MPO_x + H_2O + e^- \quad (1)$$

When adding 0.005 M N_2H_4 in electrolyte, a new oxidation peak A_2 appears in the CV curves, which is related to the preferential oxidation of N_2H_4 to the MP oxidation. The area of oxidation peak A_2 decreases with the increasing cycling number due to the decreased N_2H_4 concentration, while that of oxidation peak A_1 increases gradually because of the consumption of local N_2H_4 resulting in the following oxidation of the catalyst itself into MPO_x. In particular, the reduction peak (B_1) disappears in N_2H_4-containing electrolyte even under the existence of oxidation peak A_1, indicating that no MPO_x species is present on the catalyst surface, or can be spontaneously reduced back to MP, if there is any, by N_2H_4 because of its strong reductivity as shown in Eq. (2). The result suggests that the *in situ* electrochemically oxidized Ni-Co-P/NF in anodic potential range can be recovered back to active MP species again by N_2H_4.

$$MPO_x + N_2H_4 + H_2O \rightarrow MP + N_2 + OH^- \quad (2)$$

2

However, after the long-time CV measurements of Ni-Co-P/NF under a lowered N_2H_4 concentration or without N_2H_4, the HzOR activity of Ni-Co-P/NF will decline rapidly and cannot be recovered even at increased N_2H_4 concentration in the following (Fig. S19), which is due to the over-oxidation of catalyst (named Ni-Co-P/NF-inactivated) leading to the deactivation of Ni-Co-P/NF in the absence of N_2H_4. From the XPS spectra of Ni-Co-P/NF-inactivated (Fig. 5b, Fig. S20c, d), it can be found that the ratio of MPO_x to MP significantly increased, proving the over-oxidation of Ni-Co-P/NF responsible for the deteriorated HzOR performance, further confirming that the MP is the active sites for HzOR, which can be *in situ* recovered by N_2H_4 molecules in the electrolyte in the case of being transiently oxidized of MP.

In order to further exploring these changes, *in situ* Raman measurements were carried out. In 1 M KOH electrolyte, the catalyst Ni-Co-P/NF shows a significantly broadened band at around 400 cm^{-1} corresponding to the vibration of M – P bond[43]. When adding 0.1 M N_2H_4 in electrolyte, three strong N_2H_4 related peaks appear at 677, 1116, 1598 cm^{-1} (Fig. 5c), respectively assigned to N – H, N – N stretching modes of adsorbed $*NH_2NH_2$, and N – H bending modes of intermediate $*NH_2$ on the Ni-Co-P/NF surface[44–46]. Fig. 5d shows the real-time Raman spectra at varied applied voltages for monitoring the catalytic process by Ni-Co-P/NF for HzOR in 1 M KOH + 0.1 M N_2H_4 (-0.05 V to 0.5 V vs. RHE). At the voltage higher than 0.1 V, the peak density of M – P (400 cm^{-1}) gradually becomes weakened with the increase of voltage, and a weak peak appears near 980 cm^{-1} assigned to the stretching bond of P – O in MPO_x, indicating that part of MP species is gradually oxidized to MPO_x during the HzOR[47]. From the *in situ* Raman measurements at varied reaction time intervals at constant 0.2 V (Fig. 5e), when the voltage application was stopped for 10 minutes, the peak intensity of M-P bond (400 cm^{-1}) increased again, while the peak of P – O bond (980 cm^{-1}) disappeared, confirming that the slightly oxidized species (MPO_x) could be reduced and recovered back to active MP species due to the presence of N_2H_4, which agrees well with the CV measurement in Fig. 5a.

Furthermore, with the increase of applied voltage from – 0.05 V to 0.5 V (Fig. 5d), the N_2H_4 adsorption peak becomes gradually decreased, indicating that the surface adsorbed N_2H_4 is consumed rapidly leading to the fast HzOR kinetics of Ni-Co-P/NF. However, when the applied voltage is greater than 0.2V, the peak of $*NH_2$ becomes stronger because of the accumulation of reaction intermediate $*NH_2$, indicating the existence of another HzOR path at 0.2 V and above. That is to say that the N_2H_4 molecule may firstly be adsorbed on the bimetallic sites of Ni-Co-P/NF to form $*NH_2NH_2$, in which the N – N bond will break to form two $*NH_2$. Then, each $*NH_2$ gradually dehydrogenates to form N_2. This HzOR path is similar to the reaction mechanism on the surface of noble metals[48,49].

DFT calculations were adopted to analyze the HzOR electrocatalytic thermodynamics and kinetics. A microstructure of NiCoP/CoP heterointerface (named as < NiCoP|CoP>) was constructed virtually to simulate the Ni-Co-P/NF catalyst as shown in Fig. S21. The density of states (DOS) of the < NiCoP|CoP>

(Fig. S22) shows clearly the metallic nature, and the d-band center is located at -1.549 eV (spin-up) and −1.384 eV (spin-down), which are close to the values of other heterostructures enabling excellent bifunctional activity[50]. From the Bader charge analysis (Fig. S23), it can be found that more charges from Co than Ni can transfer to P, specifying the site preference for phosphides adsorption onto the heterostructure. Thus, different adsorption sites for N_2H_4 were examined including NiCoP-side, CoP-side and < NiCoP|CoP> (Fig. S24). Obviously, the ΔG_{*N2H4} value of < NiCoP|CoP> (-0.85 eV) indicates the highly favorable $*N_2H_4$ adsorption kinetics on the heterostructure for HzOR. Furthermore, the charge density difference analysis shows that the N atom in $*N_2H_4$ has a significant charge transfer to the nearby Co and Ni atoms, leading to the bond length increasing and the resultant activation of $*N_2H_4$ molecules(Fig. S25)[51].

It has been reported that the oxidation of N_2H_4 on the catalyst surface is usually a four-continuous-step proton coupled electron transfer (PCET) process[52,53]. Therefore, the free energies of dehydrogenation in each step at the < NiCoP|CoP > were calculated as shown in Fig. 5f. The rate-determining step (RDS) for HzOR is the dehydrogenation from $*NH_2NH_2$ to $*NHNH_2$, and the ΔG value of this step on the heterostructure is as low as 0.10 eV, indicating that the NiCoP/CoP heterointerface can offer a fast kinetics for HzOR by effectively modulating the electronic structure. Besides this, according to the *in situ* Raman spectroscopic result, another theoretically possible reaction path is proposed: $*N_2H_4 \rightarrow 2*NH_2 \rightarrow 2*NH \rightarrow 2*N \rightarrow N_2$. To verify the feasibility of this speculation, the free energies in each step were calculated as shown in Fig. 5g. At U = 0 V, the N − N bond breakage (ΔG = 0.45 eV) forming $*NH_2NH_2$ is the RDS, while the N − H bond is much easier to break. However, with the increase of the potential to 0.2 V (U = 0.2 V), the N atoms can be more strongly bound onto the catalyst surface, leading to the much lowered ΔG value down to 0.05 eV, implying the greatly weakened N − N bonding, therefore in this case, HzOR may follow a new reaction path of N-N bond breaking in hydrazine molecules in addition to the traditional four-continuous-step PCET path.

(a) LSV curves of the electrolyzer equipped with different electrode catalysts in 1 M KOH without or with the addition of N_2H_4 at anode; (b)The proposed competing electroless decomposition path (red, path 1) and electrochemical path for H_2 production from hydrazine (green, path 2); (c) Relationship between gas volume and transferred charge number at anode and cathode under different anodic N_2H_4 concentrations; (d) Stability measurements at 100 mA cm^{-2} with the ADTs in the inset; (e) Discharge polarization curve and power density plots; (f) Schematic illustration of a HE unit self-powered by a home-made DHzFC for H_2 production; (g) Digital photograph of H_2 production system with HE unit self-powered by DHzFC.

HE Unit Powered by DHzFC. Considering the excellent electrocatalytic performance of the Ni-Co-P/NF for both HER and HzOR, a H-type double-chamber electrolyzer (HE unit) was assembled using the Ni-Co-P/NF as both cathodic and anodic catalysts. The HE unit takes 1.0 M KOH + 0.1 M N_2H_4 and 1 M KOH as the anodic and cathodic electrolytes, respectively, separated by anion exchange membrane (AEM). The

separation design can avoid the pollution of N_2H_4 to the cathode solution to obtain high-purity H_2 at cathode. As shown in Fig. 6a, a current density of 200 mA cm^{-2} can be obtained at the cell voltage of 0.88 V when using Ni-Co-P/NF as electrodes for HE unit, while it can only reach 50 mA cm^{-2} under the same voltage by using Pt-C/NF electrodes (Fig. 6a). In sharp contrast, the traditional OER + HER requires 1.92 V to achieve 200 mA cm^{-2}, which is 1.04 V higher than that with Ni-Co-P/NF electrodes (0.88 V) under the same conditions, indicating the greatly reduced energy consumption by using HzOR assistant hydrogen production.

When no voltage is applied, the HE unit still exhibits an open circuit voltage (OCV) of -0.1 V and current output (Fig. S26), indicating the spontaneous H_2 evolution in the device. As a matter of fact, both HzOR and HER will take place concurrently on the Ni-Co-P/NF catalyst surface in anode chamber (Fig. 6b, path 1), leading to the electroless “spontaneous decomposition” of N_2H_4 without current (electron) output towards cathode, which is actually not desirable for anode N_2H_4 oxidation-coupled cathode HER, but widely ignored and indeed inevitable[54]. In order to further study this phenomenon, the gases produced at the cathode and anode were collected by drainage collection method to analyze the actual utilization rates of N_2H_4 (Fig. S27). The electroless “spontaneous decomposition” of N_2H_4 can be inhibited by controlling the N_2H_4 concentration as shown in Fig. 6c, so as to promote the electrochemical oxidation rate of N_2H_4 (Fig. 6b path 2). The "spontaneous decomposition" can be largely prevented at the N_2H_4 concentrations lower than 0.05 M, and in this case the electrochemical utilization rate of N_2H_4 (in path 2 in Fig. 6b) reaches 93.0%. Comparatively, the “spontaneous decomposition” reaction will take place vigorously at increased N_2H_4 concentrations, and the utilization rates of N_2H_4 were calculated to 90.5% and 67.6% at 0.1 M and 0.2 M N_2H_4, respectively.

The HE unit exhibits excellent stability for H_2 evolution (Fig. 6d), and the current density of 100 mA cm^{-2} can be driven at the voltage lower than 0.63 V and operated stably for nearly 30 h. Even after ADTs for 10000 cycles, the performance at the current density of 100 mA cm^{-2} attenuates by only 11.6% according to the inset in Fig. 6d. The regular voltage fluctuations in the stability curve in Fig. 6d mainly comes from the supplementations of N_2H_4 and the release of bubbles on the electrode (Fig. S28). Because of the large resistance (17 Ω) of AEM, the performance of Ni-Co-P/NF in HE unit has been operated with iR compensation (Fig. S29), which shows a high current density of 500 mA cm^{-2} at 0.498 V, higher than the reported capacities of HzOR-assisted HER in membrane-free or double-chamber electrolyzer (Table S5).

Based on the excellent HzOR performance of Ni-Co-P/NF, a direct hydrazine fuel cell (DHzFC) equipped with Ni-Co-P/NF as the anode immersed in 1.0 M KOH + 0.1 M N_2H_4 electrolyte and 20 wt.% Pt/C as cathode immersed in 1.0 M KOH electrolyte was constructed. As show in Fig. 6e, the DHzFC exhibits a peak power density of 96 mW cm^{-2} at 0.75 V, which can drive the LED by two identical DHzFC in series (Fig. S30). Moreover, the DHzFC can run stably at the current densities of 1, 5, 10 and 15 mA cm^{-2} for 4 h (Fig. S31), indicating its excellent operation stability at high output voltages. Furthermore, a self-powered

H_2 production system has been constructed by integrating a DHzFC and the HE unit using Ni-Co-P/NF as the bifunctional catalysts (Fig. 6f). The self-made DHzFC successfully drives the HE unit for H_2 production, resulting in the production of a large number of bubbles (see the Movie in SI), and the H_2 evolution current is as high as 26.2 mA (Fig. 6g), corresponding to a hydrogen generation rate up to 19.6 mol h^{-1} m^{-2}, proving the great potential in the utilization of self-powered hydrogen production during the non-carbon energy system.

Conclusions

An interface engineering strategy has been developed to synthesize a heterostructure nanoarrays electrocatalyst (Ni-Co-P/NF) featuring CoP nanoparticles being uniformly distributed outside of the NiCoP nanowires, which acts as a bifunctional catalyst toward both HER and HzOR. This catalyst shows extra-high HER/HzOR performances featuring especially low overpotential of 37 mV at 10 $mAcm^{-2}$ for HER, and − 54 mV and 187 mV to reach 10 mA cm^{-2} and 1000 mA cm^{-2} for HzOR, better than most reported non-noble metal or noble metal catalysts. More importantly, the catalytic mechanism of HzOR has been probed in-depth: the instant recovery of the active MP component by N_2H_4 molecules during HzOR has been confirmed, and the HzOR has been thermodynamically identified to follow a new N-N bond breakage path at 0.2 V and above beyond the traditional PCET pathway, endowing Ni-Co-P/NF with the excellent HzOR performance. Thus, the electrolyzer equipped with Ni-Co-P/NF as both anode and cathode catalysts offers as low as 0.498 V of applied voltage to reach 500 mA cm^{-2} for H_2 production, greatly reducing the energy consumption for H_2 production. Equally importantly, the electrochemical utilization rate of N_2H_4 has been determined to be as high as 93% by tuning the N_2H_4 concentration. Also interestingly, the HzOR/HER electrolyzer can be powered by DHzFC equipped with Ni-Co-P/NF as anode catalyst to realize the self-powered H_2 production at the rate up to 19.6 mol h^{-1} m^{-2}. This work provides an extra-high performance HzOR catalyst and an unusual catalytic mechanism insight, benefiting the near future industrial hydrogen production at largely lowered energy consumption.

Methods

Materials. Hydrochloric acid (HCl), Urea (99 wt.%), Hydrazine monohydrate ($N_2H_4{\cdot}H_2O$, 80 wt.%), Cobalt(II) nitrate hexahydrate ($Co(NO_3)_2{\bullet}6H_2O$, 98.5 wt.%) and Nickel(II) nitrate hexahydrate ($Ni(NO_3)_2{\bullet}6H_2O$, 98.0 wt.%) were purchased from Sinopharm Group Chemical Reagent Co., Ltd. Sodium hypophosphite (NaH_2PO_2, 99.0 wt.%) and Ammonium fluoride (NH_4F, 98 wt.%) were purchased from Aladdin. Sodium hydroxide (KOH, 90 wt.%) was purchased from Shanghai Titan Scientific Co., Ltd. Acetone, Ethanol, Isopropanol were purchased from Shanghai Lingfeng. Nafion D-520 dispersion (5 wt.%) was purchased from Dupont China Holding Co., Ltd. Commercial 20 wt.% Pt/C and the carbon black (XC-72) were purchased from Shanghai HEPHAS Energy Equipment Co., Ltd. Nickel foam (thickness: 1.0 mm; aperture: 0.1 mm; porosity: 97.2%) was purchased from Cyber Electric Co., Ltd. Anion exchange membrane (AEM,

FAB-PK-130) was purchased from Fumasep. Composite matrix was purchased from Changsha Sipulin. All materials were used as received without further purification.

Preparation of Ni-Co-P/NF electrocatalysts. The three dimensional bimetallic phosphide nanowires heterostructure nanoarrays grown in nickel foam (Ni-Co-P/NF) were synthesized by facile two-step ways[28]. In a typical synthesis, the precursor nanowire arrays (Ni-Co-Pre/NF) were *in situ* grown on substrate of nickel foam through a hydrothermal method. Nickel foam was successively washed by acetone, 1 M HCl and deionized water with ultrasonic treatment for 10 min to get rid of the possible surface greasy dirt and oxide layer. Then, 3 mmol of $Co(NO_3)_2{\cdot}6H_2O$, 10 mmol of urea and 4 mmol of NH_4F were dissolved into hydrothermal kettle lining with 60 mL of deionized water, and the pretreated nickel foam (2 cm × 3.5 cm) was put into and completely immersed in the solution. Afterward, the hydrothermal kettle was maintained at 120 ℃ for 6 h. After cooled down naturally at room temperature, the substrate was then taken out and cleaned by ultrasonic treatment with DI water and ethanol several times before being fully dried. Similarly, the different proportion of Co precursors were prepared by the same steps with the addition of $Co(NO_3)_2{\cdot}6H_2O$ differing from 1 to 5 mmol.

Bimetallic phosphide is realized by a partial phosphide reaction of the above precursor in a tubular furnace. Typically, the substrate precursor prepared above and NaH_2PO_2 were placed at two separate locations of a long crucible with NaH_2PO_2 at the upstream side of the furnace and the precursor at the other side. Then, they were heated at 325 ℃ for 4 h with a heating speed of 2 ℃ min^{-1} in N_2 atmosphere. The sample Ni-Co-P/NF was then obtained after cooling to room temperature in N_2 atmosphere.

Preparation of NiP/NF, CoP and Pt-C/NF electrocatalysts. The NiP/NF is prepared by the same method as Ni-Co-P/NF, only without adding $Co(NO_3)_2{\cdot}6H_2O$ to the precursor synthesis. The CoP is prepared by the same method as Ni-Co-P/NF, only without adding nickel foam to the precursor synthesis, which is dispersed on nickel foam during electrochemical tests.

10 mg commercial 20 wt.% Pt/C was dispersed into 970 μL isopropanol, then 30 uL 10% Nafion solution was added, and after ultrasonic the ink solution is obtained. Then 100 μL ink is uniformly applied to 1 cm^2 nickel foam and obtain the Pt-C/NF.

Materials characterization. Scanning electron microscope (SEM) imaging was obtained using a FEI Magellan-400 field emission scanning electron microscope (5 kV). Transmission electron microscopy (TEM) patterns, high-resolution transmission electron microscopy (HRTEM), energy dispersive X-ray spectrometer (EDS) and corresponding EDS-mapping were recorded on a JEM-2100F field emission transmission electron microscope (200 kV). Spherical aberration-corrected HAADF-STEM and corresponding EDS-mapping measurements were taken on a JEM-ARM300F instrument. Powder X-ray diffraction (XRD) signals were performed at 4° min^{-1} on a Rigaku D/Max-2550 V X-ray diffractometer with a Cu Kα radiation target (40 kV, 40 mA). X-ray photoelectron spectroscopy (XPS) data was tested on

Thermo Fisher Scientific ECSAlab250 XPS spectrometer with monochromatic Al K_α radiation. Raman and *in situ* Raman spectra were recorded on Raman S3 spectrometer (JY, Labram HR 800) with an excitation wavelength of 532 nm and inVia Qontorin Raman spectrometer (Renishaw).

Electrochemical measurements. All electrochemical performances were measured on a CHI 760E electrochemical workstation (CH instruments, Inc., Shanghai). Ag/AgCl electrode and carbon rod were used as reference and counter electrode, respectively. The Ag/AgCl electrode was stored in the saturated KCl solution and rinsed with deionized water before use. All the potential data reported in this work were converted to the reversible hydrogen electrode (RHE) according to the Nernst equation. All measurements related to HzOR were performed at 500 rpm to eliminate the effect of bubbles. The liner sweep voltammetry (LSV) measurements were made at the scan rate of 5 or 50 mV s^{-1}, with 90% iR compensation to eliminate the influence of solution impedance on the test results ($E_{corrrected}$ = $E_{measured}$–0.9 I*R_s, where $E_{measured}$, I and R_s are the experimentally measured potential, current and electrolyte internal resistance, respectively). The Tafel plots were obtained according to the Tafel equation η = a log|j| + b. The accelerated durability tests (ADTs) were conducted for up to 10,000 cyclic voltammetry (CV) cycles, with the voltage range from − 0.1 to 0.4 V (vs. RHE, in 1 M KOH and 0.1M N_2H_4), and − 0.3 to 0 V (vs. RHE, 1 M KOH), respectively. Electrochemical impedance spectroscopy (EIS) measurements were carried out in the frequency range from 10^{-1} to 10^{-6} Hz in different electrolytes. The electrochemical surface area (ECSA) data were calculated from CVs curves in a non-Faraday region (30–130 mV) at varied scan rates from 10 to 80 mV s^{-1} and the double-layer capacitance (C_{dl}) values with potential range of CV tests from 30 to 130 mV. The *in situ* Raman test was carried out in 1 M KOH or 1 M KOH + 0.1M N_2H_4, using the catalysts cut into 1 cm × 1 cm as work electrode and Ag/AgCl electrode as reference electrode. The electrode potential was set from − 0.05 V to 0.5 V and then was set at 0.1 V for 60 min, during which Raman test was carried out. The faradaic efficiencies (FE) of HER was calculated by the amount of charge transfer and the volume of H_2 collected by the gas gathering unit. Theoretical H_2 volume was obtained based on Faradaic law of electrolysis. Unless otherwise specialized, all the potentials are referred to the RHE and the data is not processed by iR compensation.

DFT calculation details. DFT calculations were performed using the Vienna Ab Initio Simulation Package (VASP)[55,56]. The Perdew-Burke-Ernzehof (PBE) functional and the projector augmented wave (PAW) method were applied in our calculation[57]. The < NiCoP |CoP > heterostructure was constructed by combining the NiCoP and CoP models of dozens of atoms and the lattice mismatch is around 4%. Vacuum thickness over 12 Å was applied. A kinetic energy cut-off of 520 eV and gamma K-point only were used during the structural optimization. The maximum force exerted on each atom was relaxed to less than 0.02 eV $Å^{-1}$ and the convergence criteria of energy difference is 10^{-5} eV. Dispersion correction by Grimme's DFT-D3 scheme was adopted to describe the van der Waals (vdW) interactions[58]. The free energy ΔG of intermediates is calculated following the procedure proposed by Norskov et al.[59]. The two paths of HzOR including steps of (I) $N_2H_4 \rightarrow N_2H_3 \rightarrow N_2H_2 \rightarrow N_2H \rightarrow N_2$ and (II) N_2H_4

$\rightarrow 2NH_2 \rightarrow 2NH \rightarrow 2N \rightarrow N_2$ were investigated and compared. And the free energy contributed by the electrode potential (ΔG_U) was also considered by subtracting eU from the ΔG[60].

Declarations

Acknowledgments

We sincerely appreciate the support for this research by National Natural Science Foundation of China (21835007, 52172110), Key Research Program of Frontier Sciences, Chinese Academy of Sciences (ZDBS-LY-SLH029), the “Scientific and Technical Innovation Action Plan” Hong Kong, Macao and Taiwan Science & Technology Cooperation Project of Shanghai Science and Technology Committee (21520760500), Natural Science Foundation of Shanghai (19ZR1479400), and the BL14W1 beamline of Shanghai Synchrotron Radiation Facility (SSRF).

References

1. Turner, J. A. Sustainable hydrogen production. Science **305**, 972–974, doi:10.1126/science.1103197 (2004).
2. Seh, Z. W. *et al.* Combining theory and experiment in electrocatalysis: Insights into materials design. Science **355**, doi:10.1126/science.aad4998 (2017).
3. McCrory, C. C. L., Jung, S., Peters, J. C. & Jaramillo, T. F. Benchmarking Heterogeneous Electrocatalysts for the Oxygen Evolution Reaction. Journal of the American Chemical Society **135**, 16977–16987, doi:10.1021/ja407115p (2013).
4. Fu, X. *et al.* A Self-Charging Hybrid Electric Power Device with High Specific Energy and Power. Acs Energy Letters **3**, 2425–2432, doi:10.1021/acsenergylett.8b01331 (2018).
5. Yin, P.-F. *et al.* Synthesis of Palladium-Based Crystalline@Amorphous Core-Shell Nanoplates for Highly Efficient Ethanol Oxidation. Adv. Mater. **32**, doi:10.1002/adma.202000482 (2020).
6. Li, D.-N., Wang, A.-J., Wei, J., Zhang, Q.-L. & Feng, J.-J. Facile synthesis of flower-like Au@AuPd nanocrystals with highly electrocatalytic activity for formic acid oxidation and hydrogen evolution reactions. International Journal of Hydrogen Energy **42**, 19894–19902, doi:10.1016/j.ijhydene.2017.05.186 (2017).
7. Tong, Y. *et al.* Oxygen Vacancies Confined in Nickel Molybdenum Oxide Porous Nanosheets for Promoted Electrocatalytic Urea Oxidation. Acs Catalysis **8**, 1–7, doi:10.1021/acscatal.7b03177 (2018).
8. You, B., Jiang, N., Liu, X. & Sun, Y. Simultaneous H2 Generation and Biomass Upgrading in Water by an Efficient Noble-Metal-Free Bifunctional Electrocatalyst. Angewandte Chemie International Edition **55**, 9913–9917, doi:10.1002/anie.201603798 (2016).
9. You, B., Liu, X., Jiang, N. & Sun, Y. A General Strategy for Decoupled Hydrogen Production from Water Splitting by Integrating Oxidative Biomass Valorization. Journal of the American Chemical Society

138, 13639–13646, doi:10.1021/jacs.6b07127 (2016).

10. Tang, C. *et al.* Energy-Saving Electrolytic Hydrogen Generation: Ni2P Nanoarray as a High-Performance Non-Noble-Metal Electrocatalyst. Angewandte Chemie International Edition **56**, 842–846, doi:10.1002/anie.201608899 (2017).
11. Liu, Y. *et al.* Manipulating dehydrogenation kinetics through dual-doping Co3N electrode enables highly efficient hydrazine oxidation assisting self-powered H2 production. Nature Communications **11**, 1853, doi:10.1038/s41467-020-15563-8 (2020).
12. Sun, Q., Wang, N., Xu, Q. & Yu, J. Nanopore-Supported Metal Nanocatalysts for Efficient Hydrogen Generation from Liquid-Phase Chemical Hydrogen Storage Materials. Adv. Mater. **32**, doi:10.1002/adma.202001818 (2020).
13. Jin, H. *et al.* Stable and Highly Efficient Hydrogen Evolution from Seawater Enabled by an Unsaturated Nickel Surface Nitride. Adv. Mater. **33**, doi:10.1002/adma.202007508 (2021).
14. Yamada, K., Yasuda, K., Tanaka, H., Miyazaki, Y. & Kobayashi, T. Effect of anode electrocatalyst for direct hydrazine fuel cell using proton exchange membrane. J. Power Sources **122**, 132–137, doi:10.1016/s0378-7753(03)00440-3 (2003).
15. Yamada, K. *et al.* Potential application of anion-exchange membrane for hydrazine fuel cell electrolyte. Electrochem. Commun. **5**, 892–896, doi:10.1016/j.elecom.2003.08.015 (2003).
16. Zhou, S. *et al.* Vacancy-Rich MXene-Immobilized Ni Single Atom as High-Performance Electrocatalyst for Hydrazine Oxidation Reaction. *Adv Mater*, e2204388, doi:10.1002/adma.202204388 (2022).
17. Zou, X. & Zhang, Y. Noble metal-free hydrogen evolution catalysts for water splitting. Chemical Society Reviews **44**, 5148–5180, doi:10.1039/c4cs00448e (2015).
18. Shi, Y. & Zhang, B. Recent advances in transition metal phosphide nanomaterials: synthesis and applications in hydrogen evolution reaction. Chemical Society Reviews **45**, 1529–1541, doi:10.1039/c5cs00434a (2016).
19. Hou, J. *et al.* Electrical Behavior and Electron Transfer Modulation of Nickel-Copper Nanoalloys Confined in Nickel-Copper Nitrides Nanowires Array Encapsulated in Nitrogen-Doped Carbon Framework as Robust Bifunctional Electrocatalyst for Overall Water Splitting. Advanced Functional Materials **28**, doi:10.1002/adfm.201803278 (2018).
20. Qiu, B. *et al.* Fabrication of Nickel-Cobalt Bimetal Phosphide Nanocages for Enhanced Oxygen Evolution Catalysis. Advanced Functional Materials **28**, doi:10.1002/adfm.201706008 (2018).
21. Wang, Z. *et al.* Copper-Nickel Nitride Nanosheets as Efficient Bifunctional Catalysts for Hydrazine-Assisted Electrolytic Hydrogen Production. Advanced Energy Materials **9**, doi:10.1002/aenm.201900390 (2019).
22. Li, Y. *et al.* Ternary NiCoP nanosheet arrays: An excellent bifunctional catalyst for alkaline overall water splitting. Nano Research **9**, 2251–2259, doi:10.1007/s12274-016-1112-z (2016).
23. Song, F. *et al.* Interfacing nickel nitride and nickel boosts both electrocatalytic hydrogen evolution and oxidation reactions. Nature Communications **9**, doi:10.1038/s41467-018-06728-7 (2018).

24. Zheng, X. *et al.* Identifying Dense NiSe2/CoSe2 Heterointerfaces Coupled with Surface High-Valence Bimetallic Sites for Synergistically Enhanced Oxygen Electrocatalysis. Adv. Mater. **32**, doi:10.1002/adma.202000607 (2020).
25. Zheng, J. *et al.* Hierarchical Porous NC@CuCo Nitride Nanosheet Networks: Highly Efficient Bifunctional Electrocatalyst for Overall Water Splitting and Selective Electrooxidation of Benzyl Alcohol. Advanced Functional Materials **27**, doi:10.1002/adfm.201704169 (2017).
26. Gu, Y. *et al.* Electronic Structure Tuning in Ni3FeN/r-GO Aerogel toward Bifunctional Electrocatalyst for Overall Water Splitting. Acs Nano **12**, 245–253, doi:10.1021/acsnano.7b05971 (2018).
27. Liu, X. *et al.* Self-powered H-2 production with bifunctional hydrazine as sole consumable. Nature Communications **9**, doi:10.1038/s41467-018-06815-9 (2018).
28. Li, J. *et al.* Hierarchical NiCoP nanocone arrays supported on Ni foam as an efficient and stable bifunctional electrocatalyst for overall water splitting. Journal of Materials Chemistry A **5**, 14828–14837, doi:10.1039/c7ta03947f (2017).
29. Yue, K. *et al.* In situ ion-exchange preparation and topological transformation of trimetal-organic frameworks for efficient electrocatalytic water oxidation. Energy & Environmental Science **14**, 6546–6553, doi:10.1039/d1ee02606b (2021).
30. Li, H. *et al.* Systematic design of superaerophobic nanotube-array electrode comprised of transition-metal sulfides for overall water splitting. Nature Communications **9**, 2452, doi:10.1038/s41467-018-04888-0 (2018).
31. Wang, H., Li, C., An, J., Zhuang, Y. & Tao, S. Surface reconstruction of NiCoP for enhanced biomass upgrading. Journal of Materials Chemistry A **9**, 18421–18430, doi:10.1039/d1ta05425b (2021).
32. Liu, H. *et al.* Robust NiCoP/CoP Heterostructures for Highly Efficient Hydrogen Evolution Electrocatalysis in Alkaline Solution. Acs Applied Materials & Interfaces **11**, 15528–15536, doi:10.1021/acsami.9b00592 (2019).
33. Surendran, S., Shanmugapriya, S., Sivanantham, A., Shanmugam, S. & Selvan, R. K. Electrospun Carbon Nanofibers Encapsulated with NiCoP: A Multifunctional Electrode for Supercapattery and Oxygen Reduction, Oxygen Evolution, and Hydrogen Evolution Reactions. Advanced Energy Materials **8**, doi:10.1002/aenm.201800555 (2018).
34. Boppella, R., Tan, J., Yang, W. & Moon, J. Homologous CoP/NiCoP Heterostructure on N-Doped Carbon for Highly Efficient and pH-Universal Hydrogen Evolution Electrocatalysis. Advanced Functional Materials **29**, doi:10.1002/adfm.201807976 (2019).
35. Lin, Y. *et al.* Construction of CoP/NiCoP Nanotadpoles Heterojunction Interface for Wide pH Hydrogen Evolution Electrocatalysis and Supercapacitor. Advanced Energy Materials **9**, doi:10.1002/aenm.201901213 (2019).
36. Zhao, D. *et al.* Alkali-induced 3D crinkled porous Ti3C2 MXene architectures coupled with NiCoP bimetallic phosphide nanoparticles as anodes for high-performance sodium-ion batteries. Energy & Environmental Science **12**, doi:10.1039/c9ee00308h (2019).

37. Wang, Y. *et al.* Visible-light-induced unbalanced charge on NiCoP/TiO2 sensitized system for rapid H-2 generation from hydrolysis of ammonia borane. Applied Catalysis B-Environmental **260**, doi:10.1016/j.apcatb.2019.118183 (2020).
38. Zhang, H. *et al.* Bifunctional Heterostructure Assembly of NiFe LDH Nanosheets on NiCoP Nanowires for Highly Efficient and Stable Overall Water Splitting. Advanced Functional Materials **28**, doi:10.1002/adfm.201706847 (2018).
39. Yu, J. *et al.* Ternary Metal Phosphide with Triple-Layered Structure as a Low-Cost and Efficient Electrocatalyst for Bifunctional Water Splitting. Advanced Functional Materials **26**, 7644–7651, doi:10.1002/adfm.201603727 (2016).
40. Meng, G. *et al.* Ru to W electron donation for boosted HER from acidic to alkaline on Ru/WNO sponges. Nano Energy **80**, doi:10.1016/j.nanoen.2020.105531 (2021).
41. Chen, Y. *et al.* V2C MXene synergistically coupling FeNi LDH nanosheets for boosting oxygen evolution reaction. Applied Catalysis B-Environmental **297**, doi:10.1016/j.apcatb.2021.120474 (2021).
42. Li, W. *et al.* Facile synthesis of three-dimensional structured carbon fiber-NiCo2O4-Ni(OH)2 high-performance electrode for pseudocapacitors. Scientific Reports **5**, 9277, doi:10.1038/srep09277 (2015).
43. Lyu, Y. *et al.* Identifying the Intrinsic Relationship between the Restructured Oxide Layer and Oxygen Evolution Reaction Performance on the Cobalt Pnictide Catalyst. Small **16**, doi:10.1002/smll.201906867 (2020).
44. Chellappa, R., Dattelbaum, D., Daemen, L. & Liu, Z. in *18TH APS-SCCM AND 24TH AIRAPT.* PTS 1–19 (2014).
45. Fu, Y. *et al.* Dual-metal-driven Selective Pathway of Nitrogen Reduction in Orderly Atomic-hybridized Re2MnS6 Ultrathin Nanosheets. Nano Letters **20**, 4960–4967, doi:10.1021/acs.nanolett.0c01037 (2020).
46. Lan, J. *et al.* Nanoporous B13C2 towards Highly Efficient Electrochemical Nitrogen Fixation. Small **17**, doi:10.1002/smll.202102814 (2021).
47. Xu, W. *et al.* Nanoporous Palladium Hydride for Electrocatalytic N-2 Reduction under Ambient Conditions. Angew. Chem.-Int. Edit. **59**, 3511–3516, doi:10.1002/anie.201914335 (2020).
48. Alberas, D. J., Kiss, J., Liu, Z. M. & White, J. M. SURFACE-CHEMISTRY OF HYDRAZINE ON PT(111). Surface Science **278**, 51–61, doi:10.1016/0039-6028(92)90583-r (1992).
49. Rosca, V. & Koper, M. T. M. Electrocatalytic oxidation of hydrazine on platinum electrodes in alkaline solutions. Electrochimica Acta **53**, 5199–5205, doi:10.1016/j.electacta.2008.02.054 (2008).
50. Qian, Q. *et al.* Artificial Heterointerfaces Achieve Delicate Reaction Kinetics towards Hydrogen Evolution and Hydrazine Oxidation Catalysis. Angewandte Chemie International Edition **60**, 5984–5993, doi:10.1002/anie.202014362 (2021).
51. Sun, F. *et al.* Energy-saving hydrogen production by chlorine-free hybrid seawater splitting coupling hydrazine degradation. Nature Communications **12**, 4182, doi:10.1038/s41467-021-24529-3 (2021).

52. Liu, Q. *et al.* Low-coordinated cobalt arrays for efficient hydrazine electrooxidation. Energy & Environmental Science, doi:10.1039/d2ee01463g (2022).
53. Qian, Q. *et al.* Phase-Selective Synthesis of Ruthenium Phosphide in Hybrid Structure Enables Efficient Hybrid Water Electrolysis Under pH-Universal Conditions. Small **18**, doi:10.1002/smll.202200242 (2022).
54. Li, J. *et al.* Elucidating the Critical Role of Ruthenium Single Atom Sites in Water Dissociation and Dehydrogenation Behaviors for Robust Hydrazine Oxidation-Boosted Alkaline Hydrogen Evolution. Advanced Functional Materials **32**, doi:10.1002/adfm.202109439 (2022).
55. Kresse, G. & Furthmuller, J. Efficient iterative schemes for ab initio total-energy calculations using a plane-wave basis set. Physical Review B **54**, 11169–11186, doi:10.1103/PhysRevB.54.11169 (1996).
56. Kresse, G. & Hafner, J. AB-INITIO MOLECULAR-DYNAMICS SIMULATION OF THE LIQUID-METAL AMORPHOUS-SEMICONDUCTOR TRANSITION IN GERMANIUM. Physical Review B **49**, 14251–14269, doi:10.1103/PhysRevB.49.14251 (1994).
57. Blochl, P. E. PROJECTOR AUGMENTED-WAVE METHOD. Physical Review B **50**, 17953–17979, doi:10.1103/PhysRevB.50.17953 (1994).
58. Grimme, S., Antony, J., Ehrlich, S. & Krieg, H. A consistent and accurate ab initio parametrization of density functional dispersion correction (DFT-D) for the 94 elements H-Pu. Journal of Chemical Physics **132**, doi:10.1063/1.3382344 (2010).
59. Norskov, J. K. *et al.* Origin of the overpotential for oxygen reduction at a fuel-cell cathode. Journal of Physical Chemistry B **108**, 17886–17892, doi:10.1021/jp047349j (2004).
60. Rao, R. R. *et al.* Towards identifying the active sites on RuO2(110) in catalyzing oxygen evolution. Energy & Environmental Science **10**, 2626–2637, doi:10.1039/c7ee02307c (2017).

Figures

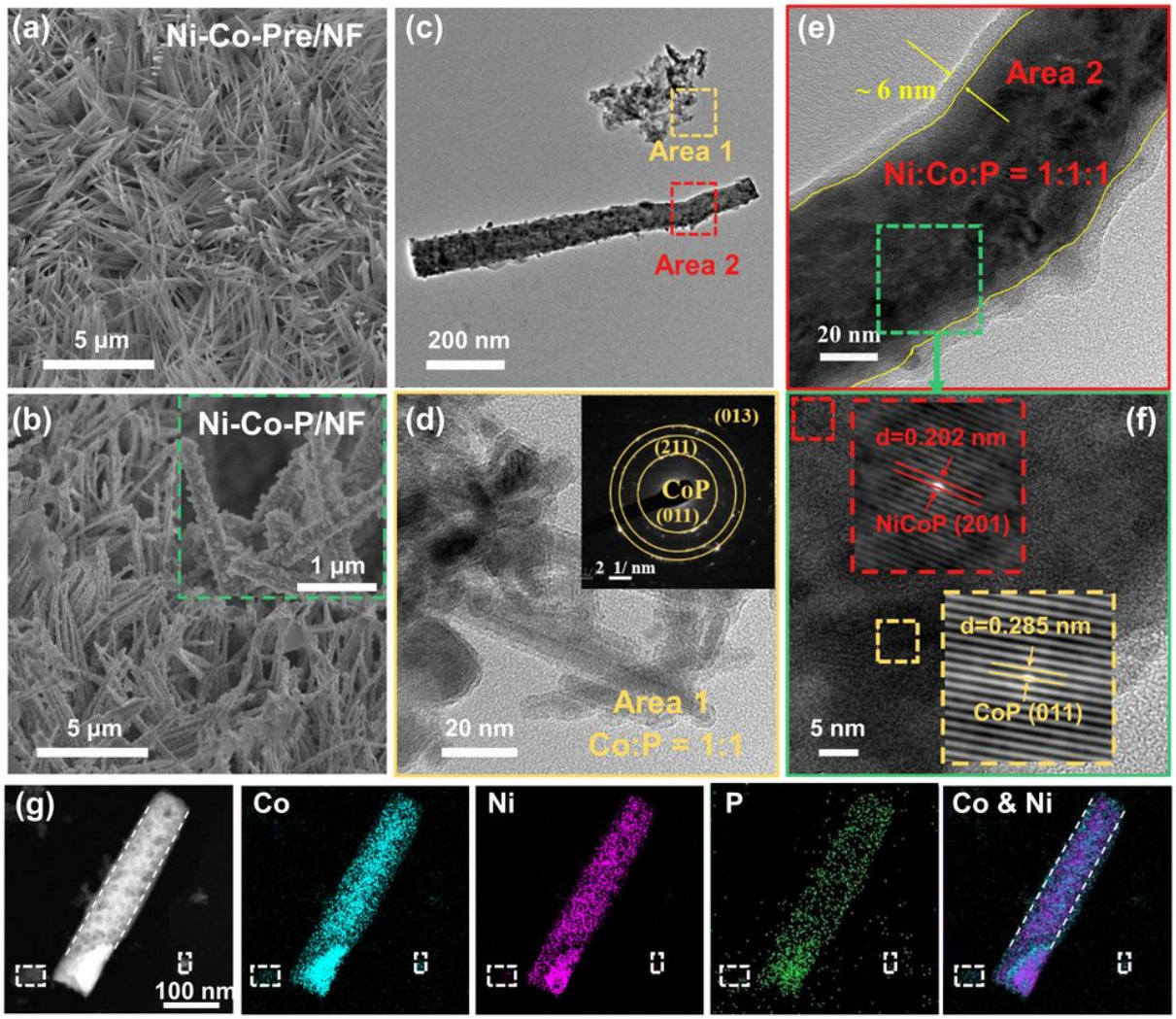

Figure 1

SEM images of (a) Ni-Co-Pre/NF and (b) Ni-Co-P/NF with a magnified image in the inset; (c) TEM image of Ni-Co-P/NF, in which the squared Area 1 and Area 2 are magnified and shown respectively in (d) and (e) with a FFT pattern of the Area 1 in the inset of (d); (f) HRTEM image of the Ni-Co-P/NF with a further magnified image in the inset; (g) STEM-EDX elemental mapping of Ni-Co-P/NF.

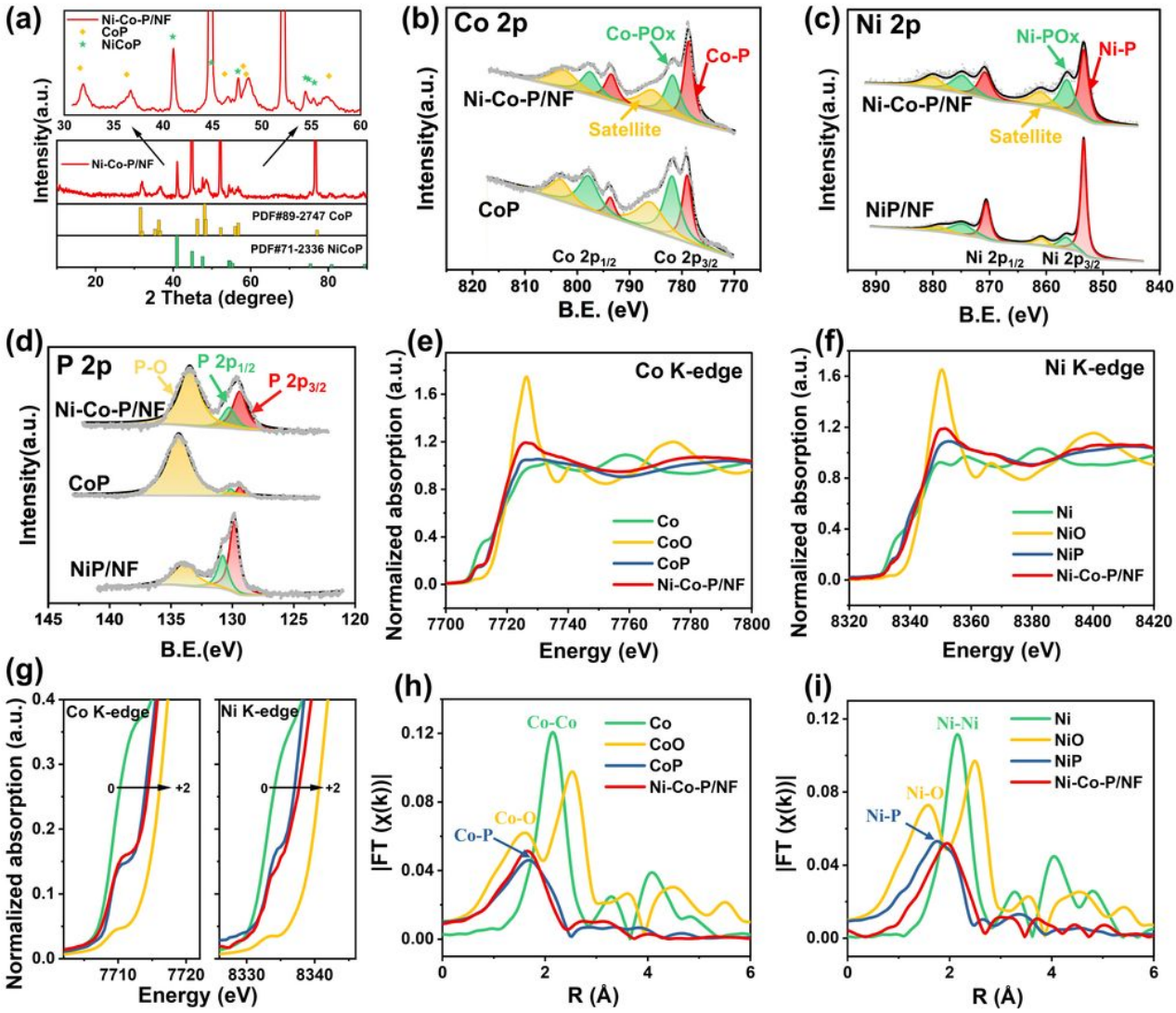

Figure 2

(a) XRD patterns of Ni-Co-P/NF; High-resolution XPS spectra of (b) Co 2p; (c) Ni 2p; (d) P 2p for the prepared samples; (e) Co and (f) Ni K-edge XANES spectra of Ni-Co-P/NF and the reference compounds; (g) the left and right correspond to the squared areas in (e) and (f), respectively; EXAFS results of (h) Co K-edge; (i) Ni K-edge for Ni-Co-P/NF and the reference compounds.

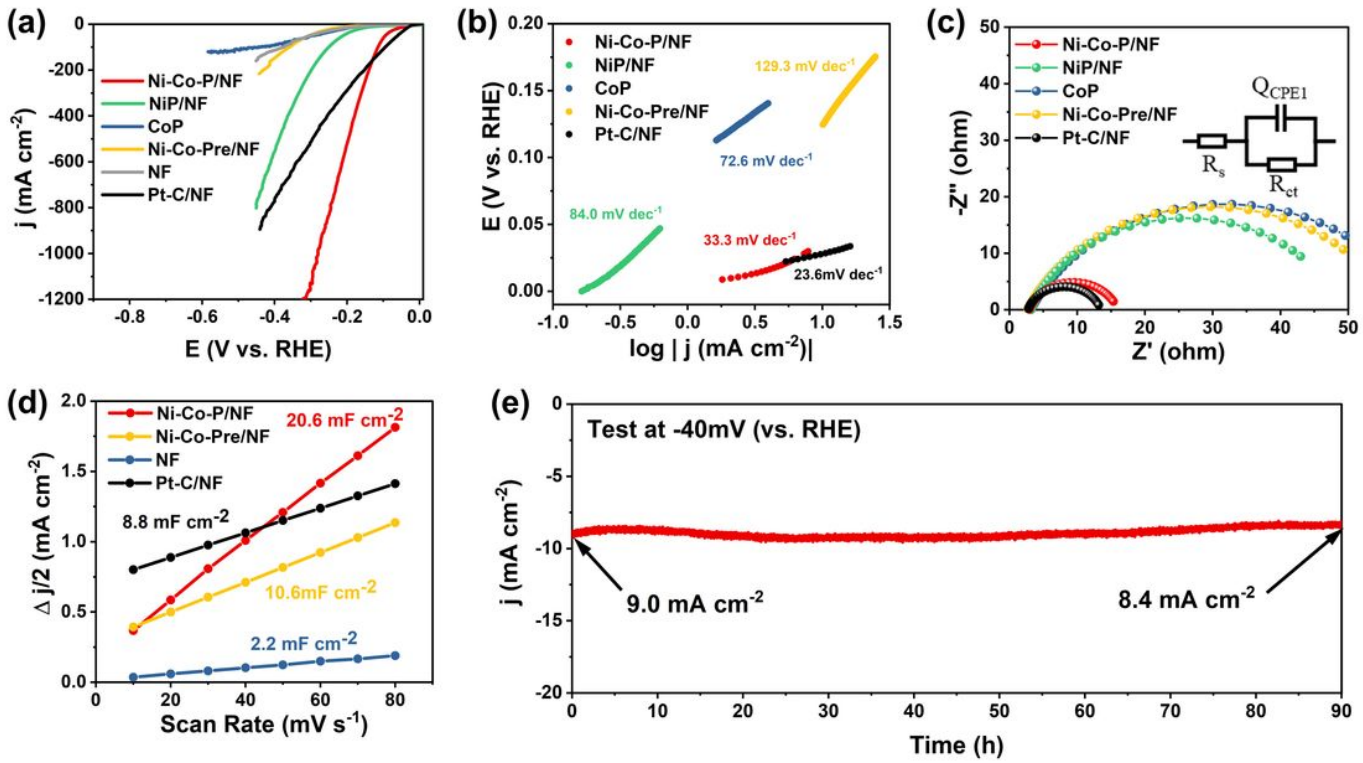

Figure 3

Electrochemical properties of HER in N_2-saturated 1.0 M KOH. (a) 90% iR-corrected LSV curves at scan rate of 5 mV s^{-1}; (b)Tafel plots; (c) Nyquist plots with the fitting pattern in the inset; (d) Double-layer capacitance C_{dl}; (e) Stability measurement of Ni-Co-P/NF.

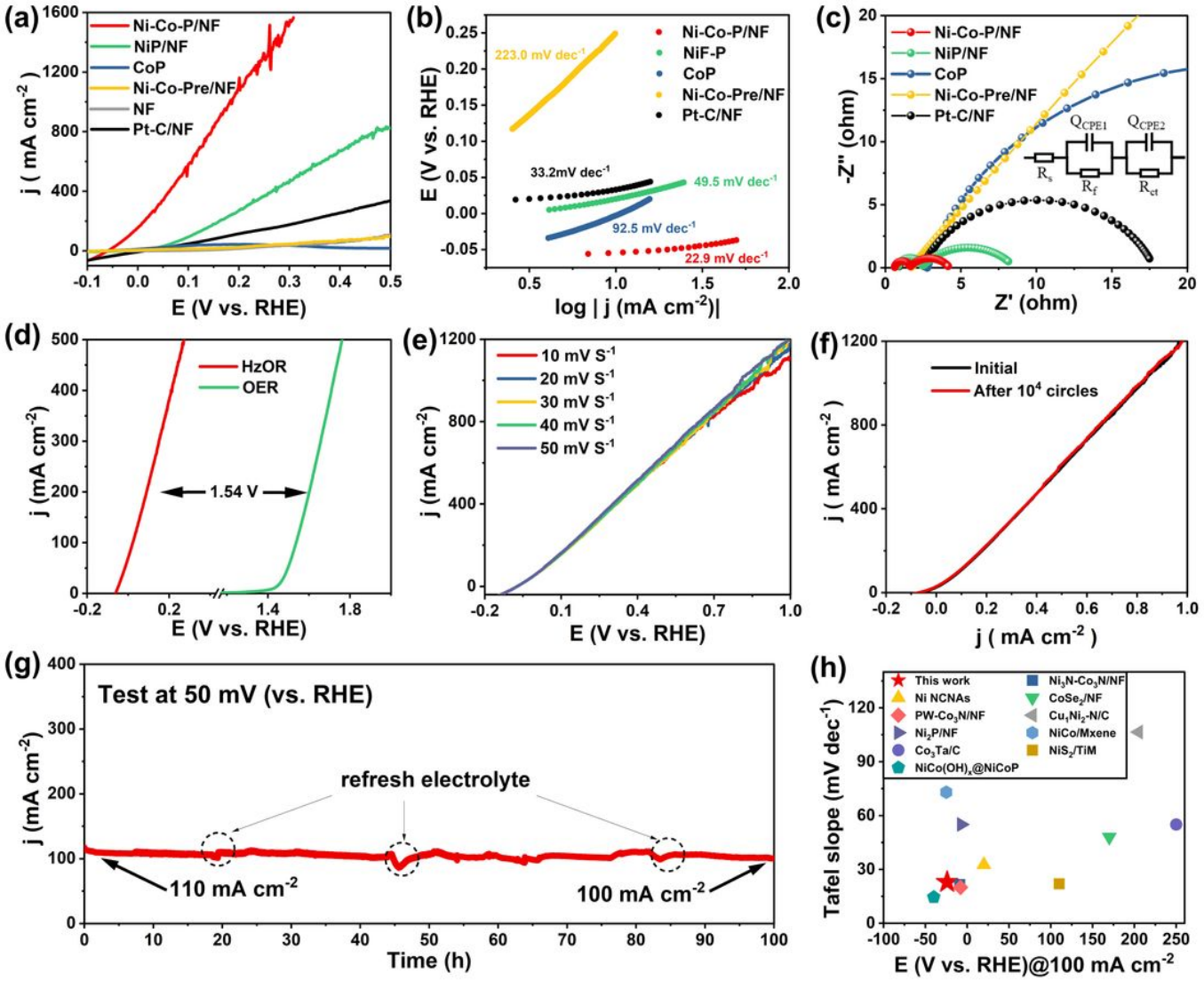

Figure 4

Electrochemical properties of the HzOR in 1.0 M KOH and 0.1 M N_2H_4. (a) 90% iR-corrected LSV; (b) Tafel slope plots; (c) Nyquist plots with the fitting pattern in the inset; (d) Polarization comparison between HzOR of Ni-Co-P/NF and OER of RuO_2; (e) LSV curves of Ni-Co-P/NF varying with scanning speed; (f) LSV curves of Ni-Co-P/NF before and after ADTs; (g) Stability measurements of Ni-Co-P/NF for HzOR; (h) Comparison of the potentials at 100 mA cm^{-2} and Tafel slopes between Ni-Co-P/NF in this work and various non-noble metal-based catalysts reported.

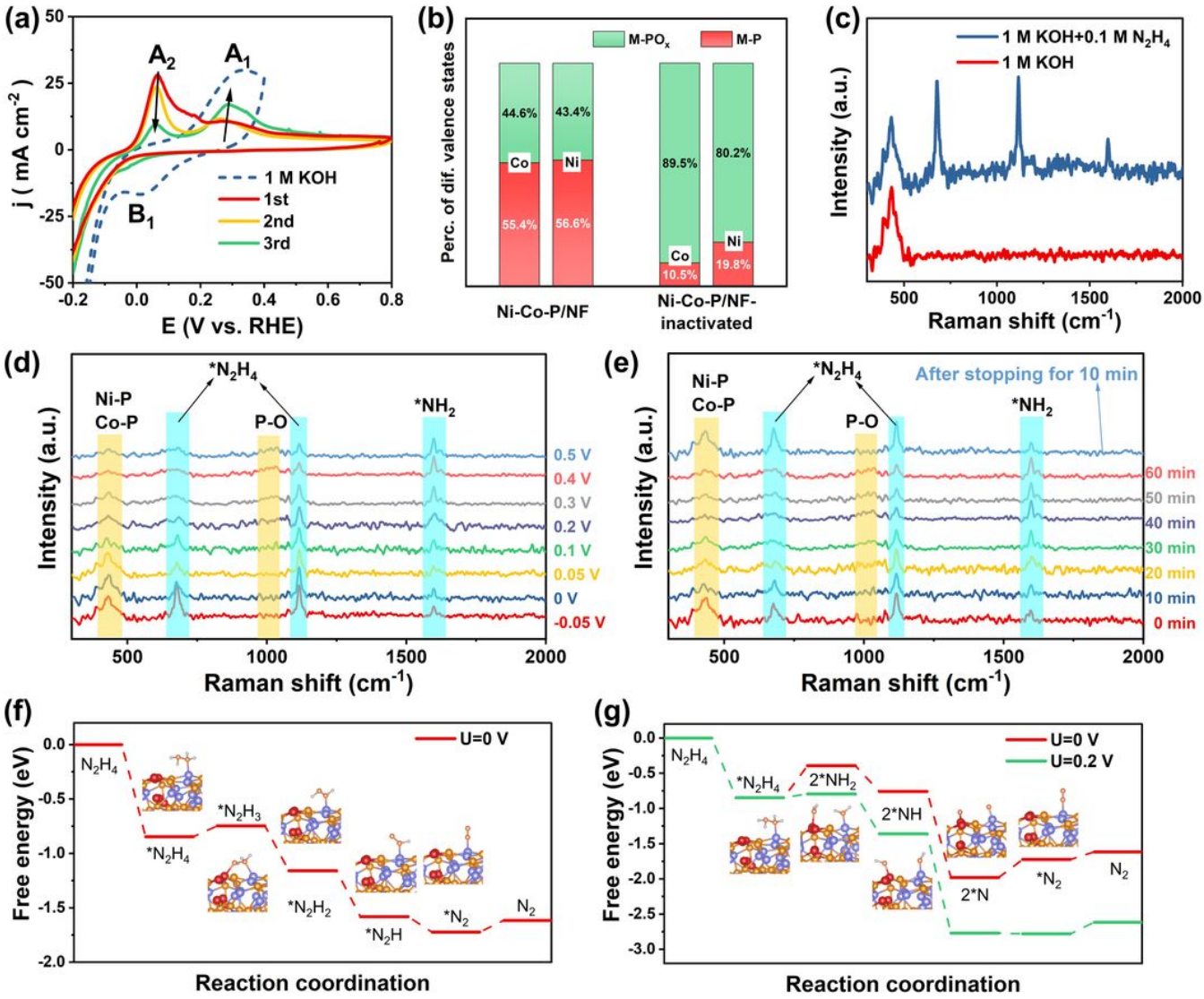

Figure 5

Catalytic mechanism of HzOR and the catalyst's evolution during catalysis. (a) CV curves in 1 M KOH (blue curves) or 1.0 M KOH + 0.005 M N_2H_4 under different cycles of scanning (red: first cycle, yellow: second cycle and green: third cycle); (b) Histograms of the ratio between MPO_x and MP for Ni-Co-P/NF and Ni-Co-P/NF-inactivated; (c) Raman spectra of Ni-Co-P/NF in 1 M KOH or 1 M KOH+0.1 M N_2H_4; (d, e) *In situ* electrochemical Raman spectra of Ni-Co-P/NF in 1 M KOH+0.1 M N_2H_4 (d) at varied applied potentials and (e) at different reaction time intervals under constant 0.2 V; (f, g) Free energy changes of HzOR in (f) path and (g) path on NiCoP/CoP heterostructure and the most stable adsorption configuration of the intermediate.

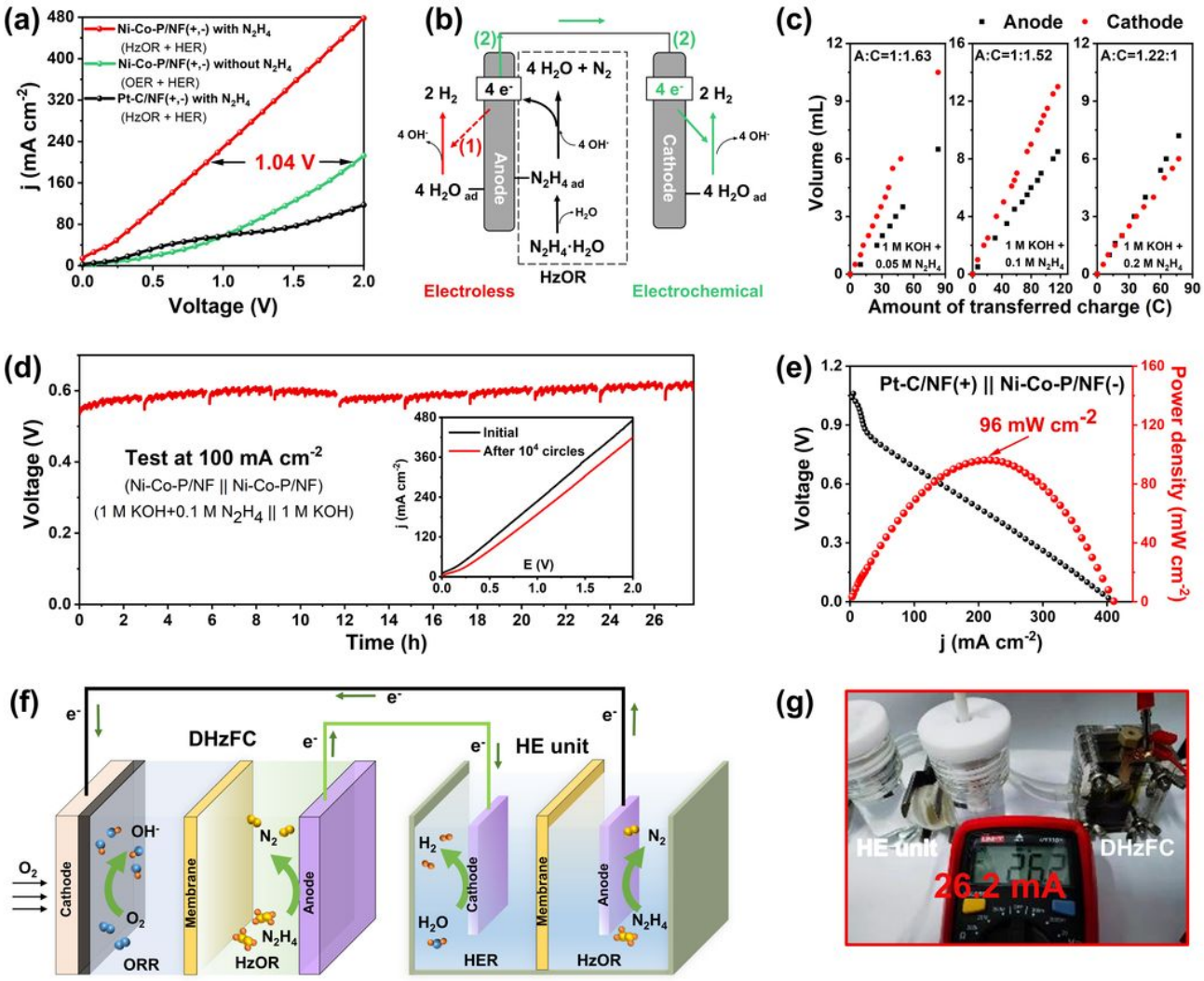

Figure 6

Electrochemical properties of the **HE unit (a, b, c, d)** with Ni-Co-P/NF as both anode and cathode catalysts; **DHzFC (e)** with Ni-Co-P/NF as anode and Pt-C/NF as cathode; **Self-powered System (f, g)**.

(a) LSV curves of the electrolyzer equipped with different electrode catalysts in 1 M KOH without or with the addition of N_2H_4 at anode; (b)The proposed competing electroless decomposition path (red, path 1) and electrochemical path for H_2 production from hydrazine (green, path 2); (c) Relationship between gas volume and transferred charge number at anode and cathode under different anodic N_2H_4 concentrations; (d) Stability measurements at 100 mA cm^{-2} with the ADTs in the inset; (e) Discharge polarization curve and power density plots; (f) Schematic illustration of a HE unit self-powered by a home-made DHzFC for H_2 production; (g) Digital photograph of H_2 production system with HE unit self-powered by DHzFC.

Supplementary Files

This is a list of supplementary files associated with this preprint. Click to download.

- Movie.mp4
- SupportingInformationforManuscript.docx